Biophysical Journal Volume 94 March 2008 2374–2384

Agnostic Particle Tracking for Three-Dimensional Motion of Cellular Granules and Membrane-Tethered Bead Dynamics

Kalpit V. Desai,* T. Gary Bishop,† Leandra Vicci,† E. Timothy O'Brien Sr.,‡ Russell M. Taylor 2nd,† and Richard Superfine‡

*Department of Biomedical Engineering, †Department of Computer Science, and ‡Department of Physics and Astronomy, The University of North Carolina at Chapel Hill, Chapel Hill, North Carolina

ABSTRACT The ability to detect biological events at the single-molecule level provides unique biophysical insights. Back-focal-plane laser interferometry is a promising technique for nanoscale three-dimensional position measurements at rates far beyond the capability of standard video. We report an in situ calibration technique for back-focal-plane, low-power (nontrapping) laser interferometry. The technique does not rely on any a priori model or calibration knowledge, hence the name "agnostic". We apply the technique to track long-range (up to 100 μm) motion of a variety of particles, including magnetic beads, in three-dimensions with high spatiotemporal resolution (~2 nm, 100 μs). Our tracking of individual unlabeled vesicles revealed a previously unreported grouping of mean-squared displacement curves at short timescales (<10 ms). Also, tracking functionalized magnetic beads attached to a live cell membrane revealed an anchorage-dependent nonlinear response of the membrane. The software-based technique involves injecting small perturbations into the probe position by driving a precalibrated specimen-mounting stage while recording the quadrant photodetector signals. The perturbations and corresponding quadrant photodetector signals are analyzed to extract the calibration parameters. The technique is sufficiently fast and noninvasive that the calibration can be performed on-the-fly without interrupting or compromising high-bandwidth, long-range tracking of a particle.

INTRODUCTION

The ability to precisely determine the position of vesicles, organelles, or particles is indispensable for the field of biophysics. In contrast to imaging techniques that provide ensemble-averaged measurements (e.g., fluorescence recovery after photobleaching), particle tracking provides insights into local characteristics of a heterogeneous environment. The first usage of particle tracking in biology was demonstrated by Crick et al. in 1950 (1) in a work employing several seminal paradigms. They used cinemicrography to measure angular displacements of magnetic particles engulfed by fibroblasts. The approach was also adopted by Yagi et al. (2) and Abercrobie et al. (3) to investigate properties of amoeba protoplasm and fibroblast locomotion, respectively. The first use of single-particle tracking (SPT) using computer-enhanced video recording was reported by Webb and collaborators, who tracked fluorescently labeled low-density lipoprotein receptors in human fibroblast cell membranes (4). Since then, SPT has quickly become widely used for microscopic position measurements in biology. De Brabander et al. developed Nanovid ultramicroscopy, a technique for tracking colloidal gold particles of 20–40 nm diameter. They used the technique for tracking endocytosis and the motion of proteins on the surface of cell membranes (5). Sheetz and collaborators developed particle-tracking techniques based on differential interference contrast microscopy to track the motion of motor molecules and membrane proteins with nanometer resolution (6). High-speed video with colloidal gold particles was used by Fujiwara et al. (7) and Murase et al. (8) to track tagged lipids within a cell membrane with a spatial precision of 17 nm at a sampling rate of 40 kHz. Selvin and collaborators developed fluorescent imaging with 1 nm accuracy, i.e., FIONA, a method for tracking a single fluorophore by fitting a Gaussian model of the point-spread function to the image of the fluorophore (9). This method offers spatial resolution of 1.5 nm and temporal resolution of 0.5–0.1 s, which they used for investigating molecular-motor activities (10).

Most of these techniques were applicable for position detection only in the focal plane of the camera. Speidel et al. (11) developed a tracking technique using epifluorescence video imaging in off-focus mode, which enabled particle tracking in the axial direction (up to 3 μm) with 100 ms temporal resolution. Video-based tracking is fundamentally limited by the number of detected photons; so spatial resolution varies inversely with the frame rate (12). The first three-dimensional (3D) particle tracking in cells was reported by Kao et al., who used an epifluorescence microscope with a cylindrical lens in the detection optics in conjunction with a computer-controlled fine focus to monitor motion of single fluorescent particles (13). Recently, Gratton and collaborators reported a laser-based feedback mechanism in which a beam continuously orbits, circular in xy and steps in z, around the particle. The center of the orbit is dynamically adjusted to keep the photomultiplier tube signal minimized, and the location of the center is used as the measurement of particle position. They applied the technique to track fluorescent particles in 3D with spatial resolution of 20 nm and temporal resolution of 30–60 ms (14).

Submitted June 3, 2007, and accepted for publication October 5, 2007.

Address reprint requests to Kalpit V. Desai, E-mail: kvdesai@gmail.com.

Editor: Gaudenz Danuser.

0006-3495/08/03/2374/11 $2.00

doi: 10.1529/biophysj.107.114140

Back-focal-plane laser interferometry

As the demand for higher spatiotemporal resolution pushes beyond the limits of video tracking, back-focal-plane laser interferometry is emerging as a promising technique for 3D position detection. This technique was first developed to measure the position of a particle inside an optical trap (15), and recently its use for position detection at low, nontrapping power has also been reported (16). In this method, a probe placed in the focus of a coherent laser beam causes light scattering, and an interference pattern between scattered and unscattered light is produced. A quadrant photodetector (QPD) placed at the back-focal-plane of the objective outputs four electrical signals as a function of the light intensity. Because the operable volume of the interferometric detection system by itself is smaller than 1 μm^3, position feedback is often added to keep the probe centered in the laser. Position feedback is implemented either by moving the specimen relative to the laser using a specimen-translation stage or by moving the laser relative to the specimen using acousticoptical deflectors. In theory, for particles within limits of the Raleigh scatterer, sums and differences of the individual quadrant signals give the 3D position of the particle with subnanometer accuracy at bandwidths limited only by the detector electronics (up to 1 MHz). Rohrbach and collaborators have also developed rigorous mathematical methods for mapping four QPD signals into 3D probe position (referred to as Q-to-P map or F_{QP}) for probes larger than Raleigh scatterers (17,18). The interpretation of QPD signals, as offered by the theoretical models, becomes increasingly complex for particles larger than a Raleigh scatterer.

Theoretical models also assume dielectric particles or, at best, particles with a uniform refractive index. It has been shown by simulations that the F_{QP} quickly departs from the linear differences-and-sums relationship for gold particles even with sizes smaller than the Raleigh scatterer (19). To the best of our knowledge, no such analytical model for magnetic particles, with metallic inclusions inside dielectric enclosures, has been reported. Magnetic tweezers, a technique gaining wide popularity among biophysicists (1,20–29), requires magnetic probes for force application. The ability to track magnetic beads with laser interferometry promises synergistic advantages for enabling a wide range of experiments. Our custom-built 3D force microscope (3DFM) (23) was designed as a flexible biological force instrument and hence required the development of a technique for tracking magnetic beads over long ranges.

Traditionally, F_{QP} is calibrated by fitting analytical models to volumetric scan data that are acquired by raster scanning a probe (affixed to the specimen) across the laser beam waist. Because the probe of interest may be different from the probe used to determine F_{QP}, probe-to-probe variations significantly compromise the accuracy of position detection. To avoid probe variation artifacts, Lang et al. fitted multivariate nonlinear polynomials as F_{QP} for each probe of interest (16). Here, a high-power laser was used to trap and scan a dielectric particle in the focal plane of a low-power laser, and the calibration of the detector over that plane was then used for position detection in two dimensions (2D). The laser trap as a translation technique is most applicable in the case of a trappable probe in samples of low viscosity where the probe will follow the trap motion simply and on fast timescales. This technique would not work, for example, in cases where the probe cannot be trapped or is affixed to or is inside a cell. Furthermore, laser trapping can cause unwanted heating (30–32).

In this report, we present agnostic tracking, a software-based in situ calibration technique that significantly relaxes constraints on shape, size, composition, and environment of the probe. The technique does not rely on prior knowledge of the scattering function, hence the name ''agnostic''. The technique uses a single low-power, nontrapping laser and a means to move the probe within the scattering laser detection volume with nanoscale accuracy, either a nanometric stage or a calibrated laser deflection system. We inject known perturbations into the probe position relative to the laser and analyze the QPD response to the perturbations to determine the F_{QP} for those particular experimental conditions and circumstance. We demonstrate the versatility of the technique by tracking the 3D motion of unlabeled vesicles moving inside living cells and tracking magnetic beads attached to live cell membranes.

Vermeulen et al. (33) recently reported a technique that bears similarities to our approach, e.g., they also calibrated the detector response in situ by quickly moving the trapping laser across the bead. Although they also appreciated the need for recalibrating the detector during an experiment, their approach required interruption of the experiment to allow the recalibration. In contrast, we perform recalibration on-the-fly and do not cause any interruption in the ongoing experiment. Additional improvements reported here in comparison to their approach include the ability of 3D position detection; accounting for nonlinearities of the detector response; increased accuracy of on-the-fly calibration due to cancellation of Brownian motion; and the use of low-power nontrapping laser, allowing the use of a magnetic bead as the probe.

METHODS

Instrumentation of the interferometric tracking system

We used an 825 nm, 36 mW fiber-coupled diode laser (model IFLEX1000-P-2-830-0.65-35-N; Point Source, Southampton, England) for position detection. Laser power at the specimen plane was ~25 μW. The forward scattered light was detected by a Quadrant Photo Diode (model QD-.05-0-SD; Centrovision, Newbury Park, CA), modified to have a 40 kHz cutoff frequency. A three-axis closed-loop nanopositioning stage (model Nano-LP 100; Mad City Labs, Madison, WI) was used for computer-controlled specimen-translations relative to the laser. For further details, please refer to our previous instrumentation work (23).

Coordinate frames and related notations

We were primarily interested in measuring the motion of the probe relative to the specimen; this may be caused by diffusion, local interactions, and ex-

ternal forces. In laser interferometry, the motion of the probe relative to specimen, at short timescales, causes small excursions away from the laser center. These excursions can be measured by a QPD provided that F_{QP} is calibrated. Because the laser interferometry detection system by itself can function only within $<350\ nm^3$ volume of the focused laser beam waist, the tracking of longer range excursions must be assisted by a specimen-translation stage driven by a computer-based feedback controller. The controller software moves the stage (and thus the specimen) relative to the laser to keep the probe within the operable range of the laser. It is therefore convenient to establish two coordinate frames, one centered in the laser and one attached to the specimen (Fig. 1). The position of the probe with respect to the specimen ($\vec{P}_L(t)$) can be determined from the independent measurements of the probe with respect to the laser ($\vec{P}_L(t)$), and the position of the specimen stage with respect to the laser ($\vec{S}_L(t)$) through Eq. 1, given below. The former is obtained from the scattered light signal at the QPD, and the latter is obtained from the nanometric stage sensor recordings.

$$\vec{P}_S(t) = \vec{P}_L(t) - \vec{S}_L(t) \tag{1}$$

During feedback, $\vec{S}_L$ tends to compensate for the long timescale components of $\vec{P}_S$, whereas $\vec{P}_L$ is essentially the quick motion that is left uncompensated, i.e., the error signal of the feedback loop. Thus, $\vec{S}_L$ reflects the low-frequency (i.e., within loop bandwidth) components of $\vec{P}_S$, whereas $\vec{P}_L$ contains the high-frequency components of $\vec{P}_S$.

The mechanical response of the stage shows a roll-off at ~30 Hz and hits a noise-limited measurement floor at 550 Hz. Thus the stage-sensor signals beyond 550 Hz contain little true motion information and are dominated by electrical noise. Therefore, we digitally filtered the stage-sensed positions ($\vec{S}_L$) with a 600 Hz low-pass cutoff filter.

In situ calibration of F_{QP} for each probe of interest (offline case)

At the beginning of each experiment, the user drives the stage to put the probe of interest at the center of the laser. This alignment is aided primarily by a continuously updating display of the interference pattern incident on the QPD. Once this coarse alignment is achieved, a calibration of F_{QP} begins by moving the probe within the scattering laser. Because we must begin with feedback off, we require that the bead does not drift appreciably during the initial calibration procedure. This constraint is considerably relaxed in our subsequent discussion. We refer to this as ''offline'' calibration. Later we discuss ''on-the-fly'' calibration, in which the calibration of F_{QP} is performed while position feedback is operational. To obtain a calibration of F_{QP}, we moved the probe with respect to the scattering laser by injecting perturbations to the stage position and fit a parametric model of F_{QP} to the data acquired during perturbations. We observed that a second-order polynomial adequately described F_{QP} within the local region, as the coefficients for the polynomial did not significantly change for higher order polynomial fits. To avoid co-linearities between regressor variables, we centralized the QPD signals and limited the polynomials to second order (34). Thus, F_{QP} is a group of three polynomials, one for each axis:

$$F_{QP_x}{:}P_{Lx}(Q'_1,\ldots,Q'_4) = \sum_{i=1}^{4}\left[\beta_i^x Q'_i + \sum_{j=i}^{4}\beta_{ij}^x Q'_i Q'_j\right], \tag{2}$$

where

$$Q'_k = Q_k - \mu[Q_k] = Q_k - Q_k^0.$$

Using Eq. 1 and related notations, we construct the block diagram for offline calibration of F_{QP} as shown in Fig. 2. Note that the F_{PQ} block bundles up several physical processes, i.e., scattering, interference, and light detection by the QPD. Naturally, the true F_{PQ} is unobservable and so is the true F_{QP}. The procedure for extracting F_{QP} from the measured signals is presented formally in the Appendix.

Design of the perturbation signals for offline calibration of F_{QP}

To establish the relationship between movement of the probe in 3D and changes in QPD outputs, we needed to acquire a set of data consisting of the four QPD signals at a set of 3D coordinates within the region where we wished to establish feedback and determine the position of the bead. The choice of the stage motion to acquire this data set needs to be considered. We chose to move the stage through a set of coordinates determined by three statistically independent random sequences, one for each axis. We do not perform a raster scan, as this raises the danger of confusing time-dependent signals (drift) as a spatially dependent signal. It is known that the true F_{QP} is single valued only within a small region of the beam waist. The size of that region, i.e., 200–350 nm in diameter (16), sets the upper bound to the perturbation amplitude. Within this limit, higher amplitude perturbations are always preferred because a larger operable neighborhood reduces the burden on the feedback controller. Typically, we set the amplitude of perturbations

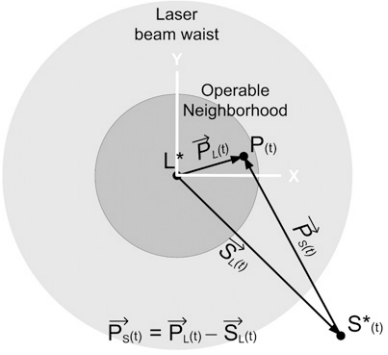

FIGURE 1 Coordinate frames. Two coordinate frames are defined: one with its origin at L* is fixed relative to the laser beam waist; the other with its origin at S* is fixed relative to the specimen. The specimen translates with the stage, so S* moves relative to L* during the experiment. The L and S frames are mutually congruent and differ only in translation. Probe position P is measured in the L frame as P_L and can be calculated in the S frame as $\vec{P}_S = \vec{P}_L + \vec{L}_S$, where $\vec{L}_S = L^* - S^*$. Provided that P is kept within the operable neighborhood of the laser (indicated by the *inner circle*), $\vec{P}_S(t) = \vec{P}_L(t) - \vec{S}_L(t)$ holds true during the entire course of an experiment.

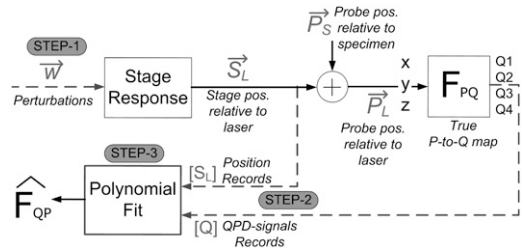

FIGURE 2 Block diagram of F_{QP} calibration procedure (offline case). To initialize the calibration procedure, perturbations are injected into the drive signal of the stage, which causes perturbations in the probe position relative to laser. The small changes in the probe position cause small changes in the QPD signals according to F_{PQ}, the true P-to-Q map. Using acquired QPD signals and stage positions as the input-output data, three second-order polynomials in centralized QPD signals are regressed, one for each axis of motion. A family of the three polynomials comprises $\hat{F}_{QP}$, the estimated Q-to-P map. This is used to measure the probe position relative to the laser, which is also the error signal for the position feedback loop that is trying to keep the probe centered in the laser.

to 50 nm, giving 100 nm as the diameter of the operable neighborhood. As shown in the Appendix, variance in the estimated coefficient is given by:

$$\sigma^2[\hat{\beta}_k^x|\bar{R}_k] = \frac{\sigma^2[\bar{\varepsilon}_x'|\bar{R}_k] + \sigma^2[\bar{P}_{xk}|\bar{R}_k]}{\sum_{n=0}^{N} R_{k\langle n\rangle}^2}, \quad (3)$$

$\hat{\beta}_k^x$: k^{th} element of the estimated regression-coefficient vector $\bar{\beta}^x$

$\bar{R}_k$: k^{th} column of the regressor matrix $\bar{\mathbf{R}}$

for a linear F_{QP}, because $|R_k| \propto |\vec{W}|$, the denominator of Eq. 3 increases quadratically with the perturbation amplitude. Thus, in addition to providing a larger operable neighborhood, higher amplitude perturbations also produce a more precise estimate of F_{QP}.

Also, for a linear F_{QP}, the N-point summation term in the denominator can be approximated by a χ^2 distribution, the mean of which increases with N. Thus, longer duration perturbations would give a more precise estimate of F_{QP}. However, for offline calibration, longer durations may let the probe diffuse out of the single-valued region. For significantly mobile probes, it is therefore preferable to keep the duration of perturbations as short as possible. With the offline calibration established as ''good enough'' to initiate feedback, we can then move on to a description of on-the-fly calibration that allows highly mobile probes. Because a feedback loop usually operates with a large gain margin, scaling-type errors in the estimate of F_{QP} are tolerable for maintaining stable feedback. At a system noise of ~10 nm root mean square, for probes moving with velocities up to ~1 μm/s, we were able to achieve stable feedback using an estimate of F_{QP} obtained from a calibration procedure lasting 100 ms.

Once an offline estimate of F_{QP} is available and position feedback is initiated, the probe is kept relatively centered at the focus of the laser. If F_{QP} is to be recalibrated while in feedback, the feedback alleviates the drawbacks of uncontrolled external disturbances ($\vec{P}_S$), e.g., diffusion, in two ways. First, because the bead is kept centered within laser, perturbations can be injected for longer durations, thus increasing the denominator in Eq. 3. Second, because the feedback compensates for the slow motion of the probe relative to the laser, the disturbance seen by the detector is reduced, thus reducing the second term in the numerator. Each of these effects produces a more precise estimate of F_{QP}.

An additional motivation for on-the-fly calibration arises from the fact that the true F_{QP} depends on the refractive index of the environment. To investigate the importance of this dependence, we carried out a simulation based on Mie scattering theory for plane waves as presented in Born and Wolf (35) for a 1-μm diameter sphere with a refractive index of 1.5 in an 830 nm coherent laser beam. For refractive indices in the range relevant to the cytoplasm, we observed (data not shown) that the scattering field changes by ~500% for a 10% change in the refractive index of the environment. Because the QPD signals depend quadratically on the scattering field (17,36), a change in the refractive index of the environment may dramatically change the QPD response. As a simpler example, Vermeulen et al. have reported that the calibration parameters change significantly with the distance from a glass surface (33). Moreover, the errors introduced due to the outdated calibration of the QPD may remain hidden from the user. That is because for a feedback loop operating with a sufficient gain margin, the errors in the sensor (QPD) signals must be exceedingly large to cause loop instabilities. With a stable position feedback loop, the user may not get an indication about an inaccurate QPD calibration that could compromise the quantitative position information in the high frequency error signal ($\vec{P}_L$).

Therefore, if the probe is moving through optically heterogeneous environments, it is necessary to recalibrate F_{QP} frequently. Tracking long-range motion of the probe requires uninterrupted use of position feedback; so the recalibration must be performed on-the-fly, without interrupting the ongoing experiment.

On-the-fly calibration

When perturbations are injected while operating in feedback, the measured stage position is a combination of the stage-response to two signals: feedback controller effort and perturbations. For the purpose of calibrating F_{QP}, components associated with perturbations must be extracted from the measured stage positions. A system without memory can be completely identified using perturbations that are limited to single frequency. Also, sinusoids of a single frequency can be extracted from a noisy signal simply by using correlation-based template matching. Thus, no knowledge of the stage impulse response or feedback loop transfer function is necessary. We chose sinusoidal perturbations to simplify the on-the-fly calibration procedure. Simultaneous calibration of F_{QP} for all three axes of motion can be achieved by selecting three coprime numbers as the frequencies of the sinusoids. Because the perturbations are also subject to suppression by the feedback loop, the selected frequencies should be outside the bandwidth of the feedback loop, which is 30 Hz in our case. We chose 67, 61, and 53 as the perturbation frequencies for the x, y, and z axes, respectively.

RESULTS

Performance evaluation of agnostic tracking

Two experimental results demonstrate the flexibility and the spatiotemporal resolution offered by agnostic tracking. For the first experiment, 14 paramagnetic, 1-μm diameter beads diffusing freely in 2 M sucrose solution were tracked individually. All beads were chosen to be far enough from the glass surfaces to avoid wall effects (37). Mean-squared displacement (MSD) analysis was carried out for the 3D trajectory of each bead. Fig. 3 shows the MSD of one such bead with bars signifying standard error over the whole ensemble. The tight error bars suggest consistency and reproducibility of the position measurement technique. As would be expected for free diffusion in a Newtonian fluid (38), the MSD

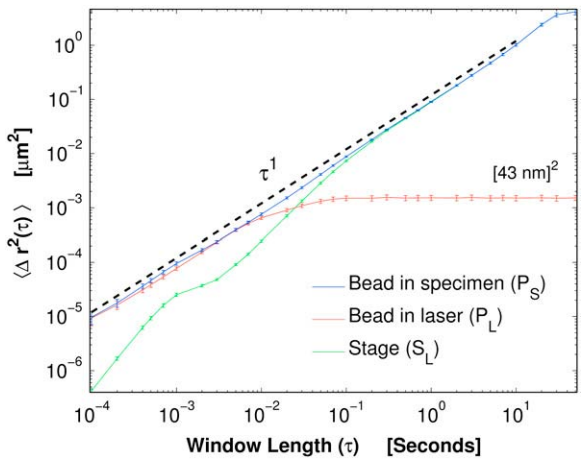

FIGURE 3 Performance evaluation by tracking Brownian motion. An ensemble of 14 beads (paramagnetic, 1 μm diameter) freely diffusing in 2 M sucrose were tracked in 3D at 10 kHz using agnostic tracking. MSD analysis was carried out for three signals: bead position relative to specimen (*blue*), bead position relative to laser (*red*), and stage position (*green*). The curves represent MSDs obtained from the trace of one such bead, and the error bars represent standard error over the ensemble.

of the bead position relative to specimen approximately follows unity power law (0.997 ± 0.004). Also, the viscosity estimate obtained using the Stokes-Einstein relationship (39) is 0.021 ± 0.001 Pa-S, which is in excellent agreement with the theoretical value 0.0212 for 2 M sucrose at room temperature (25°C) (40). These agreements between established standards and measured values imply that the position measurement bandwidth is at least as high as 10 kHz; it could be higher for higher sampling rates. The crossover of MSD curves indicates that the feedback loop bandwidth is ~30 Hz, which is primarily limited by the response of the specimen-translation stage.

The second experiment was aimed toward determining a), the spatial resolution of agnostic tracking; and b), the amount of contamination, if any, caused by perturbations injected for on-the-fly calibration. A 1 μm bead diffusing in a 2 M sucrose solution was tracked while sinusoidal perturbations were injected in stage positions. The second half of the acquired data was used to obtain a new calibration of F_{QP}, and the first half was used as the test bed for the thus obtained $\hat{F}_{QP}$. For the test bed data, $\vec{P}_L$ was computed by evaluating the new $\hat{F}_{QP}$ at the measured QPD signals. Because at this spatial scale we can ignore inertia and do not expect the stage perturbations to cause probe motion within the specimen, an increase in $\vec{P}_S$ during perturbations can only be attributed to inaccuracies of on-the-fly calibration and measurement artifacts introduced thereof. Fig. 4 shows $\vec{P}_S, \vec{P}_L$, and $\vec{S}_L$ immediately before and after the perturbations were initiated. Using the correlation between $\vec{P}_S$ and the perturbations, we found that 2% of perturbations were visible in $\vec{P}_S$. So, for perturbations of 50 nm amplitude, the error introduced during perturbations is ~1 nm. Thus for most experiments, this error is well within the acceptable levels.

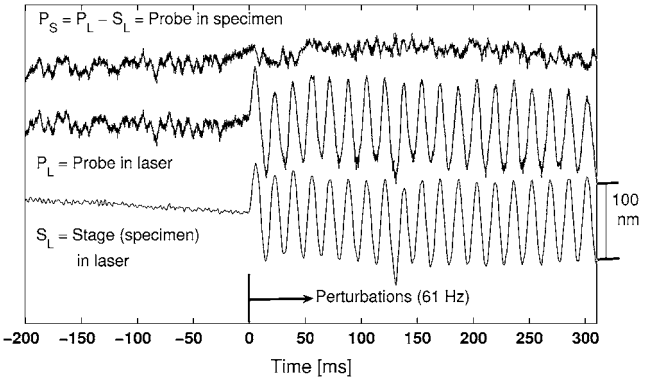

FIGURE 4 On-the-fly calibration is accurate and noninvasive. A bead diffusing in a viscous solution being tracked while sinusoidal perturbations were injected in stage positions. The latter half of the acquired data was used to obtain a new calibration of F_{QP}, and the first half was used as the test bed for the thus obtained $\hat{F}_{QP}$. $\vec{P}_L$ was obtained by evaluating the new $\hat{F}_{QP}$ at the acquired QPD signals. As shown, the perturbation sinusoids were not visible in the $\vec{P}_S$. Using correlation between $\vec{P}_L - \vec{S}_L$ and the perturbations ($\vec{W}$), we found that $\hat{F}_{QP}$ obtained on-the-fly was accurate to within 2%.

Vesicle diffusion inside live cells reveals mysterious grouping

Understanding the viscoelastic properties of cytoplasm is an active area of research in the field of biophysics. One important approach for probing properties of cytoplasm is to analyze the diffusive or molecular-motor driven motion of cytoplasmic vesicles. The particle being tracked could be a microinjected or phagocytosed bead (41–45), or it could be an endogenous vesicle (46,47) or molecule (48). Magnetic beads can also be ingested by cells and pulled by magnetic fields to study cytoplasmic response to external mechanical stimuli (2,49,50). Because neither diffusive nor driven motion is constrained to be in the image plane, 3D position detection is usually desired. Measurement of the viscoelastic modulus with high bandwidth requires high temporal resolution, whereas detection of molecular-motor steps requires nanoscale spatial resolution. We demonstrate the utility of the high spatiotemporal resolution offered by our technique for tracking 3D motion of endogenous vesicles. An added advantage of using laser-scattering based position detection is that the vesicles can be tracked in their native state without any labeling. Also, because we use a low-power laser, the natural motion of vesicles is not inhibited by optical trapping. In addition, because we use position feedback, we are able to track the long-range motion of vesicles.

We tracked 11 vesicles diffusing inside the cytoplasm of live human breast cancer (M-231) cells (Fig. 5 *A*). The MSD as a function of window length (τ) is plotted in Fig. 5 *B*. The positions of the vesicles relative to cytoplasm were recorded from the brightfield images and grouped into four categories, i.e., on cellular edge, in lamella, in perinucleus, and in perinucleolus; and a cartoon of cell (Fig. 5 *B*, *inset*) provides a visual reference for the vesicles' locations. Each MSD curve is shifted along the vertical axis such that the ensemble collapses, allowing an easier comparison of the slopes. As seen, at longer timescales ($\tau > 0.01$S) eight vesicles exhibit a power law $\alpha_1 = 0.64 \pm 0.07$, which is consistent with previously reported values for vesicle diffusion in cytoplasm, based on experiments (41,47) as well as theory (51,52). The other three vesicles exhibit a multimodal behavior where no single power law dominates. At short timescales ($\tau < 0.01$), three distinct power laws emerge: $\beta_1 = 0.49 \pm 0.18$ ($N = 3$), $\beta_2 = 0.94 \pm 0.02$ ($N = 2$), and $\beta_3 = 1.48 \pm 0.08$ ($N = 6$). Although the sample size is too small to draw reliable conclusions, we attempt a plausible explanation based on entangled polymer network theory.

For a particle diffusing in an entangled network of polymers, a 0.75 power law in the MSD plot suggests that the polymers comprising the network are semiflexible, i.e., they are characterized by a large ratio of the persistence length (L_P) to the molecular diameter (53). On the other hand, a 0.5 power law suggests that the polymers comprising the network are flexible (54,55), characterized by a smaller molecular cross section or shorter persistence length. Among the

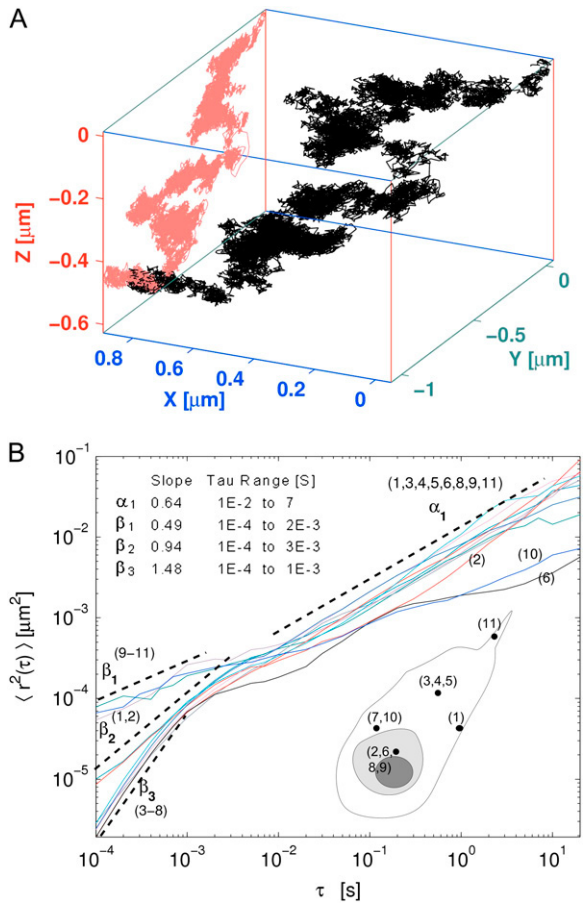

FIGURE 5 Tracking unlabeled vesicle diffusion in cytoplasm reveals grouping. Unlabeled vesicles diffusing inside live M-231 (HBC) cells were tracked in 3D using agnostic tracking. (*A*) 3D trace of the motion of one vesicle. Left panel shows projected *y-z* displacement (*red*). (*B*) MSD analysis for an ensemble of 11 vesicles. Curves were normalized by an individual scaling factor such that the ensemble collapses, allowing easier comparison of slopes. At longer timescales ($\tau > 0.01$), $\alpha_1 = 0.64 \pm 0.07$ ($N = 8$) is the primary mode. At short time scales ($\tau < 0.01$), three distinct power laws are observed: $\beta_1 = 0.49 \pm 0.18$ ($N = 3$), $\beta_2 = 0.94 \pm 0.02$ ($N = 2$), and $\beta_3 = 1.48 \pm 0.08$ ($N = 6$). The numbers in parentheses refer to the vesicles indices. (*Inset*) A cartoon grouping vesicles into four categories according to their locations in cytoplasm: near cell edge (1,11), on lamella (3–5), perinucleus (7,10), and perinucleolus (2,6,8,9).

three primary polymers present in the cytoplasm, F-actin is considered a semiflexible polymer ($L_P \approx 17$ μm), whereas microtubules are rigid filaments ($L_P \approx 6$ mm). However, some of the intermediate filaments (e.g., keratin, vimentin) have short persistence lengths and have been reported to behave as flexible polymers (56–60). The 0.49 power law (β_1) for relatively short timescales may suggest that the immediate environment of those vesicles is constituted by a network of intermediate filaments, which is further encaged by a network of F-actin or microtubules. For shorter timescales, the vesicle feels the dynamics of the network of intermediate filaments, whereas for longer timescales the vesicle diffuses farther and begins to feel the dynamics of a mixed polymer network, inducing a 0.64 (α_1) power law that is intermediate to the theoretical values of 0.5 for flexible polymer networks and 0.75 for semiflexible polymer networks. A power law close to 0.64 can be identified in the data reported by Yamada et al. (46) for the diffusion of endogenous lipid-storage granules located in COS7 lamellae. On the other hand, Caspi et al. (41) have reported superdiffusion ($\tau^{1.5}$) at short timescales, bearing a strong resemblance with the power law β_3. They suggested frequent and random interactions with molecular motors as the dominating mechanism at short timescales. They also acknowledged a strong dependence of the power law on the particle size relative to the mesh size of the surrounding network. A particle that is smaller than the mesh size is oblivious to the mesh dynamics, which may be reflected by the near-diffusion power law β_2.

Correlations between the grouping of vesicles in MSD slopes and their locations with respect to cytoplasm further suggest that the MSD slopes observed reflect properties of the environment. For example, all three vesicles located in lamella exhibit the β_3 (1.48) power law, whereas none of the two vesicles at cell boundary exhibit the β_3 power law. Also, all three vesicles that exhibit multimodal behavior at long timescales are either near to a nucleus or near to a nucleolus. Although we acknowledge that the sample size is too small to claim or contest any specific hypothesis, it is useful to note that the flexibility and resolution offered by agnostic tracking enables the detection of these fundamentally distinct phenomena.

Anchoring-dependent step response of a live cell membrane

The physical properties of the plasma membrane have been probed by a number of methods, from high speed video to the laser trap. Many interesting phenomenon have been observed, from subdiffusive to superdiffusive behavior, caused by proposed structures such as corrals and lipid rafts (61–64). We chose to look at the behavior of beads anchored either to the outer leaflet of the plasma membrane or through a transmembrane link to the cytoskeleton. We used antibodies to membrane-bound glycosylphosphatidyl inositol (GPI) anchored protein or β1 integrin transmembrane receptor to specify the type of linkage expected.

To obtain a specific linkage to GPI-anchored or β1 integrin receptors, we added biotinylated mouse anti-human CD73 (a gift from Ken Jacobson's lab, UNC-CH) antibody or β1 (CD29) antibodies to IMR-90 (human lung fibroblast) cells for 15 min, then washed and added streptavidin-coated 1-μm diameter superparamagnetic beads (Dynal, Carlsbad, CA) for 30 min (Fig. 6 *A*). These were then rinsed with medium, and the cells were placed in our magnetic stage on the 3DFM. The beads were pulled using the magnetic fields with forces between 5 pN and 30 pN, and their position was tracked in 3D at 10 kHz using agnostic tracking.

In the absence of a magnetic force, the GPI-anchored beads showed significantly higher thermal fluctuations than the

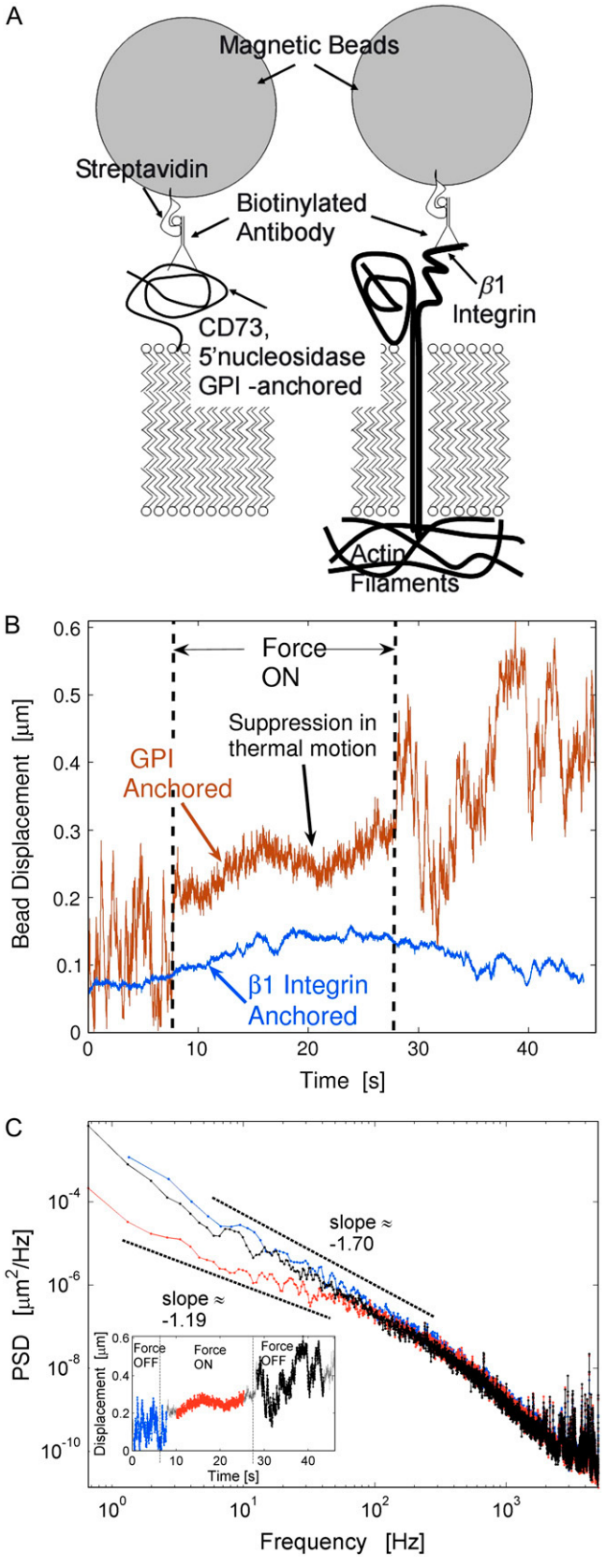

FIGURE 6 Nonlinear dynamics revealed in step response of a cell membrane. (*A*) A sketch showing the two types of superparamagnetic bead attachments used on IMR-90 cells: GPI anchored and B1-integrin anchored. Note that the GPI-anchored beads are not directly attached to the cytoskeleton, whereas the integrin-anchored beads are. The beads were pulled and their position was tracked in 3D at 10 kHz using the 3DFM. (*B*) Lateral-position traces of a GPI-anchored bead (*brown*) and an integrin-anchored bead (*blue*) as a step force was applied using magnets. Note that otherwise large thermal fluctuations of the GPI-anchored bead are suppressed when force is active. (*C*) Power spectral density curves for GPI-anchored bead position, computed over the section of the position trace that shares the same color in the inset. Note that a distinct slope ($\alpha = 1.19$) emerges when force is active.

β1 integrin-anchored beads. The difference in the amplitude of thermal fluctuations may be because the integrin receptors are directly connected to the cytoskeleton whereas the GPI anchors are not. Interestingly, the thermal fluctuations of GPI-anchored beads were greatly suppressed when magnetic force was active, whereas the integrin-anchored beads did not show any change in thermal fluctuations upon application of force (Fig. 6 *A*).

To further investigate the nature of the quick suppression of thermal fluctuations in GPI-anchored beads, we analyzed the time dependence of the power spectral density (PSD) of the bead motion. Fig. 6 *C* shows three PSD curves for the bead motion before force application, during force application, and after the force is turned off. The position trace of a GPI bead is provided in the inset. The color of a section in the inset matches the color of the associated PSD curve. The application of force caused the PSD curve to shift to an ~ -1.2 slope for lower frequencies (<100 Hz), whereas the behavior at higher frequencies (<300 Hz) remained largely unaffected. Thus the suppression of the thermal fluctuations as observed in the time domain was not distributed evenly across the whole spectrum. We note that the similar suppression observed in an optical trap is due to the nature of the effective potential seen by the particle, which in turn is imposed by the laser trap itself. In contrast, a magnetic force does not impose a potential profile of itself. Hence, the nonlinear suppression observed in our case implies a fundamental change in the environment of the bead. We hypothesize that the force pushes the bead against the barriers of the membrane skeleton; hence the dynamics of the membrane skeleton become dominant in the bead motion. As a separate observation, the suppression phenomenon may potentially be used as a test to determine whether a specific protein (i.e., the target of the bead-labeling antibody) is bound to cytoskeleton. We are investigating additional controls to further understand the mechanism behind the phenomenon.

DISCUSSION

We report an in situ and on-the-fly calibration technique of the quadrant photodetector used in back-focal-plane laser interferometry. The technique, when used in conjunction with position feedback, offers the combined advantages of

long-range tracking and high spatiotemporal resolution position detection in 3D. We note, however, that because the technique is built upon laser interferometry, it cannot be used for multiple particle tracking (MPT), for example, to study rheological coupling between different compartments of the cytoplasm. In comparison, video tracking can be used for MPT in 2D, albeit with a loss of spatiotemporal resolution. Also, laser interferometry can readily be combined with a video-imaging setup, thus integrating the contextual or global measurements from MPT along with local high spatiotemporal resolution position measurements from laser interferometry.

Because we use a specimen-translation stage in active feedback to keep the probe centered in the laser, it is important to understand if the mechanical response of the stage affects the final measurement bandwidth. For simplicity we ignore the proportional integral controller and consider the stage bandwidth to be a reasonable approximation of the feedback loop bandwidth. Hence, the stage motion compensates for the components of the probe motion up to the stage bandwidth and keeps the probe confined within a small region of the laser beam. This confinement manifests itself as a plateau at long timescales in the detected probe position within the laser (Fig. 3). The height of the plateau indicates the size of the confinement (here, an ~43 nm radius), which depends upon two parameters: the energy content of the bead motion components up to the stage bandwidth and the amount of cancellation exerted by the stage. The former depends upon the diffusion coefficient at given size, temperature, and viscosity; whereas the latter depends on the bandwidth of the stage. For a given value of these two parameters, if the size of the confinement that can be imposed by the stage is greater than the size of the operable neighborhood, the obtained $\hat{F}_{QP}$ cannot reliably map the QPD signals generated by the probe excursions outside the operable neighborhood, ultimately causing feedback disruption. This puts a lower bound on the required stage bandwidth for successfully tracking a probe with a given diffusion coefficient. As long as the stage bandwidth is higher than the bound, feedback can be successfully maintained and a further increase in the stage bandwidth would simply shift the MSD crossover (Fig. 3) without actually affecting the ultimate measurement bandwidth.

CONCLUSION

This work presents a novel approach that dramatically improves flexibility and robustness of a laser interferometric 3D position detection system. The flexibility offered enables long-range as well as high-bandwidth tracking of a variety of particles, from vesicles to beads, and the improved robustness provides accurate measurements inside live biologic environments. We demonstrated the applicability of the approach by tracking in 3D unlabeled vesicular transport inside live cells, as well as by tracking magnetic beads attached to a live cell membrane. The ability to track magnetic beads using laser interferometry offers combined advantages of magnetic force instruments with high-bandwidth position tracking. Two novel biological phenomena are revealed by application of our technique: one, grouping diffusion characteristics at short timescales (<0.01 s) for vesicles from identical cell type; and two, anchorage-dependent nonlinear dynamics of the cell membrane upon application of external force. Further investigation of each phenomenon may provide important biophysical insights.

APPENDIX

Formulation of regression equations for offline calibration of F_{QP}

We will rewrite the RHS of Eq. 2 in a compact, vector multiplication form as

$$F_{QP_x} : P_{Lx}(Q'_1, \ldots, Q'_4) = \bar{R}\bar{\beta}^x, \tag{4}$$

where

$\bar{\beta}^x$: Regression-coefficient vector, whose elements are β_i^x and β_{ij}^x terms of Eq. 2

$\bar{R}$: Regressor-variable vector, whose elements are Q′ terms of Eq. 2

Using the block diagram, we would rewrite Eq. 2 in terms of observable signals, i.e., $\vec{S}_L$ and QPD signals. Looking at the rightmost summing junction we can write

$$\vec{S}_L(t) = \vec{P}_L(t) - \vec{P}_S(t).$$

Substituting expression for $\vec{P}_L$ from Eq. 4 gives the regression equation

$$\vec{S}_L(t) = \bar{R}(t)\bar{\beta} + \vec{\varepsilon}'(t) - \vec{P}_S(t) = \bar{R}(t)\bar{\beta} + \vec{\varepsilon}(t), \tag{5}$$

where

$\vec{\varepsilon}'(t)$: Error due to noise, and deviations of the polynomial model from true F_{QP}

$\vec{\varepsilon}(t) = \vec{\varepsilon}'(t) - \vec{P}_S(t)$: The error term for regression procedure

From Eq. 5 the least-square estimate of coefficient vector $\bar{\beta}$ is given by Weisberg (65):

$$\hat{\bar{\beta}} = (\bar{\mathbf{R}}^T\bar{\mathbf{R}})^{-1}\bar{\mathbf{R}}^T\mathbf{S}_L, \tag{6}$$

where $\bar{\mathbf{R}}$ and $\mathbf{S}_L$ are the matrices comprised by stacking $\bar{R}(t)$ and $\vec{S}_L(t)$ for different values of t in each row. Once $\hat{\bar{\beta}}$ is computed, position of the probe relative to laser is estimated as

$$\hat{\vec{P}}_L(t) = \bar{R}(t)\hat{\bar{\beta}}. \tag{7}$$

Note that before application of the Eq. 7, the QPD signals must be centralized by the same Q^0 that was used to centralize the regressor variables in Eq. 1.

Regression equations for on-the-fly calibration

Because the regression process is identical for three axes, we limit our discussion to that of the x axis. Let $H(\tau)$ denote the closed-loop transfer function of the position feedback. Then,

$$\begin{aligned}\vec{P}_L(t) &= \vec{P}_S(t) \ * \ H(\tau) + \vec{W}(t) \ * \ A(\tau) \ * \ H(\tau)\\ &= \vec{P}_S(t) \ * \ H(\tau) + \hat{k}_w\sin(2\pi f_w t + \hat{\phi}_w)\end{aligned}$$

Rearranging and considering only the x axis component,

$$\hat{k}_w^x\sin\left(2\pi f_w^x t + \hat{\phi}_w^x\right) = \bar{R}(t)\bar{\beta}^x + \varepsilon_x(t)$$

Substituting expression for P_{Lx} from Eq. 2, we get the regression equation

$$\hat{k}_w^x \sin\left(2\pi f_w^x t + \hat{\phi}_w^x\right) = P_{Lx}(t) - P_{Sx}(t) \ * \ H^x(\tau), \quad (8)$$

where the error term for the regression equation is given by

$$\varepsilon_x(t) = \varepsilon_x'(t) - P_{Sx}(t) \ * \ H^x(\tau) = \varepsilon_x'(t) - p_x(t), \quad (9)$$

where

$$\varepsilon_x'(t) = \text{The error due to deviations of the polynomial model from the true } F_{QP};$$
$$p_x(t) = P_{Sx}(t) * H^x(\tau).$$

From the next section of the appendix, the variance of on-the-fly estimated coefficients is given by

$$\sigma^2\left[\hat{\beta}_k^x | \bar{R}_k\right] = \frac{\sigma^2[\bar{\varepsilon}_x' | \bar{R}_k] + \sigma^2[\bar{p}_x | \bar{R}_k]}{\sum_{n=0}^{N} R_{k\langle n\rangle^2}}. \quad (10)$$

Here the second term in the numerator has changed from $\sigma^2[\bar{P}_{Sx}|\bar{R}_k]$ in Eq. 3 to $\sigma^2[\bar{p}_x|\bar{R}_k]$. Because $p_x(t)$ is obtained by applying the filter $H^x(\tau)$ to $P_{Sx}(t)$, $\sigma^2[\bar{p}_x|\bar{R}_k]$ is smaller than $\sigma^2[\bar{P}_{Sx}|\bar{R}_k]$. Thus, when the probe is highly mobile, on-the-fly calibration is more precise than offline calibration.

Bias and variance of the coefficient estimates

Considering only x axis component of Eq. 6

$$\begin{aligned}
\hat{\beta}_k^x &= \left(\bar{R}_k^T \bar{R}_k\right)^{-1} \bar{R}_k^T \bar{S}_{Lx} \\
&= \left(\bar{R}_k^T \bar{R}_k\right)^{-1} \bar{R}_k^T \left(\bar{R}_k \beta_k^x + \bar{\varepsilon}_x\right) \quad \langle \because \bar{S}_{Lx} = \bar{R}_k \beta_k^x + \bar{\varepsilon}_x \rangle \\
&= \left(\bar{R}_k^T \bar{R}_k\right)^{-1} \bar{R}_k^T \bar{R}_k \beta_k^x + \left(\bar{R}_k^T \bar{R}_k\right)^{-1} \bar{R}_k^T + (\bar{\varepsilon}_x) \\
\hat{\beta}_k^x &= \beta_k^x + \left(\bar{R}_k^T \bar{R}_k\right)^{-1} \bar{R}_k^T (\bar{\varepsilon}_x). \quad (11)
\end{aligned}$$

Taking expected values on both sides of Eq. 11

$$\begin{aligned}
E\left[\hat{\beta}_k^x | \bar{R}_k\right] &= E\left[\beta_k^x + \left(\bar{R}_k^T \bar{R}_k\right)^{-1} \bar{R}_k^T (\bar{\varepsilon}_x) \middle| \bar{R}_k\right] \\
&= \beta_k^x + \left(\bar{R}_k^T \bar{R}_k\right)^{-1} E[\bar{\varepsilon}_x | \bar{R}_k]
\end{aligned}$$

For offline calibration, $\bar{\varepsilon}_x = \bar{\varepsilon}_x' - \bar{P}_{Sx}$, so

$$E\left[\hat{\beta}_k^x | \bar{R}_k\right] = \beta_k^x + \left(\bar{R}_k^T \bar{R}_k\right)^{-1} (E[\bar{\varepsilon}_x' | \bar{R}_k] + E[\bar{P}_{Sx} | \bar{R}_k])$$

Assuming that the second-order polynomial adequately describes the true F_{QP}

$$E\left[\hat{\beta}_k^x | \bar{R}_k\right] = \beta_k^x + \left(\bar{R}_k^T \bar{R}_k\right)^{-1} E[\bar{P}_{Sx} | \bar{R}_k]. \quad (12)$$

For on-the-fly calibration, $\bar{\varepsilon}_x = \bar{\varepsilon}_x' - \bar{p}_x$

$$E\left[\hat{\beta}_k^x | \bar{R}_k\right] = \beta_k^x + \left(\bar{R}_k^T \bar{R}_k\right)^{-1} (E[\bar{\varepsilon}_x' | \bar{R}_k] + E[\bar{P}_x | \bar{R}_k])$$

Assuming that the second-order polynomials adequately describes the true F_{QP}

$$E\left[\hat{\beta}_k^x | \bar{R}_k\right] = \beta_k^x + \left(\bar{R}_k^T \bar{R}_k\right)^{-1} E[\bar{p}_x | \bar{R}_k]. \quad (13)$$

Taking variance on both sides of Eq. 11,

$$\begin{aligned}
\sigma^2\left[\hat{\beta}_k^x | \bar{R}_k\right] &= \sigma^2\left[\left(\bar{R}_k^T \bar{R}_k\right)^{-1} \bar{R}_k^T (\bar{\varepsilon}_x) \middle| \bar{R}_k\right] \\
&= \left(\bar{R}_k^T \bar{R}_k\right)^{-1} \bar{R}_k^T \sigma^2[\bar{\varepsilon}_x | \bar{R}_k] \bar{R}_k \left(\bar{R}_k^T \bar{R}_k\right)^{-1} \\
&= \sigma^2[\bar{\varepsilon}_x | \bar{R}_k] \left(\bar{R}_k^T \bar{R}_k\right)^{-1} \bar{R}_k^T \bar{R}_k \left(\bar{R}_k^T \bar{R}_k\right)^{-1} \\
&= \sigma^2[\bar{\varepsilon}_x | \bar{R}_k] \left(\bar{R}_k^T \bar{R}_k\right)^{-1} \\
&= \frac{\sigma^2[\bar{\varepsilon}_x | \bar{R}_k]}{\sum_{n=0}^{N} R_{k\langle n\rangle^2}} \quad \langle \because \bar{R}_k = R_{k_{\langle n\rangle}} \quad n = 0, 1, 2, \ldots, N \rangle
\end{aligned}$$

For offline calibration, $\bar{\varepsilon}_x = \bar{\varepsilon}_x' - \bar{P}_{Sx}$, so

$$\sigma^2\left[\hat{\beta}_k^x | \bar{R}_k\right] = \frac{\sigma^2[\bar{\varepsilon}_x' | \bar{R}_k] + \sigma^2[\bar{P}_{Sx} | \bar{R}_k]}{\sum_{n=0}^{N} R_{k\langle n\rangle^2}}. \quad (14)$$

For on-the-fly calibration, $\bar{\varepsilon}_x = \bar{\varepsilon}_x' - \bar{P}_x$

$$\sigma^2\left[\hat{\beta}_k^x | \bar{R}_k\right] = \frac{\sigma^2[\bar{\varepsilon}_x' | \bar{R}_k] + \sigma^2[\bar{p}_x | \bar{R}_k]}{\sum_{n=0}^{N} R_{k\langle n\rangle^2}}. \quad (15)$$

Extracting perturbation-associated components from stage positions

We can represent the perturbation-associated components as

$$W_x(t) \ * \ A^x(\tau) \ * \ H^x(\tau) = k_w^x \sin\left(2\pi f_w^x t + \phi_w^x\right). \quad (16)$$

where

f_w^x : Frequency of the perturbation sinusoid for the x axis
k_w^x : Amplitude of the perturbations that is visible in probe position $\hat{\vec{P}}_L$
ϕ_w^x : Phase of the perturbations that are visible in probe position $\vec{P}_L$.

Here, k_w and ϕ_w are the unknown parameters. We can find both of these parameters by correlating stage positions with sinusoid templates. If t_s is the sample interval, and N is total number of data points used for the calibration process, we can make a sinusoid template as

$$T_{xsin} = \sin(2\pi f_w^x n t_s) \quad n = 0, 1, 2, \ldots, N$$

If we define correlation function between vectors $A(n)$ and $B(n)$ as

$$\Re_{A,B}[\phi] = \sum_{n=0}^{N} (A(nt_s) - \mu[A])(B(nt_s + \phi) - \mu[B])$$

then the delay can be estimated as

$$\hat{\phi}_w^x = \arg_\phi \max\left(\Re_{S_{Lx}, T_{xsin}}[\phi]\right) \quad (17)$$

The original sinusoidal template can be adjusted for the delay as

$$T_{xsin}^{\phi} = \sin(2\pi f_w^x n t_s + \hat{\phi}_w^x) \quad n = 0, 1, 2, \ldots, N$$

Then the amplitude of perturbations can be estimated as

$$\hat{k}_w^x = \frac{\Re_{S_{Lx}, T_{xsin}^{\phi}}[\phi = 0]}{\Re_{T_{xsin}^{\phi}, T_{xsin}^{\phi}}[\phi = 0]} \quad (18)$$

Substituting expressions for k_w^x and ϕ_w^x into Eq. 16, we can accurately extract perturbation components from stage positions.

We thank the members of Ken Jacobson's lab (Universith of North Carolina-Chapel Hill) for providing us with the anti-CD73 antibody and for insightful discussions.

This work was supported by the National Institute of Biomedical Imaging and Bioengineering, including grant P41-EB002025-23A1 and grant R01-EB000761.

REFERENCES

1. Crick, F. H. C., and A. F. W. Hughes. 1949. The physical properties of cytoplasm: a study by means of the magnetic particle method. *Exp. Cell Res. Suppl.* 1:37–80.
2. Yagi, K. 1961. The mechanical and colloidal properties of amoeba protoplasm and their relations to the mechanism of amoeboid movement. *Comp. Biochem. Physiol.* 3:73–80.
3. Abercrombie, M., J. E. M. Heaysman, and S. M. Pegrum. 1970. The locomotion of fibroblasts in culture: III. Movements of particles on the dorsal surface of the leading lamella. *Exp. Cell Res.* 62:389–398.
4. Barak, L. S., and W. W. Webb. 1982. Diffusion of low density lipoprotein-receptor complex on human fibroblasts. *J. Cell Biol.* 95: 846–852.
5. Geerts, H., M. de Brabander, and R. Nuydens. 1991. Nanovid microscopy. *Nature.* 351:765–766.
6. Schnapp, B. J., J. Gelles, and M. P. Sheetz. 1988. Nanometer-scale measurements using video light-microscopy. *Cell Motil. Cytoskeleton.* 10:47–53.
7. Fujiwara, T., K. Ritchie, H. Murakoshi, K. Jacobson, and A. Kusumi. 2002. Phospholipids undergo hop diffusion in compartmentalized cell membrane. *J. Cell Biol.* 157:1071–1082.
8. Murase, K., T. Fujiwara, Y. Umemura, K. Suzuki, R. Iino, H. Yamashita, M. Saito, H. Murakoshi, K. Ritchie, and A. Kusumi. 2004. Ultrafine membrane compartments for molecular diffusion as revealed by single molecule techniques. *Biophys. J.* 86:4075–4093.
9. Yildiz, A., J. N. Forkey, S. A. McKinney, T. Ha, Y. E. Goldman, and P. R. Selvin. 2003. Myosin V walks hand-over-hand: single fluorophore imaging with 1.5-nm localization. *Science.* 300:2061–2065.
10. Yildiz, A., and P. R. Selvin. 2005. Fluorescence imaging with one nanometer accuracy: application to molecular motors. *Acc. Chem. Res.* 38:574–582.
11. Speidel, M., A. Jon, and E. L. Florin. 2003. Three-dimensional tracking of fluorescent nanoparticles with subnanometer precision by use of off-focus imaging. *Opt. Lett.* 28:69–71.
12. Carter, B. C., G. T. Shubeita, and S. P. Gross. 2005. Tracking single particles: a user-friendly quantitative evaluation. *Phys. Biol.* 2:60–72.
13. Kao, H. P., and A. S. Verkman. 1994. Tracking of single fluorescent particles in three dimensions: use of cylindrical optics to encode particle position. *Biophys. J.* 67:1291–1300.
14. Levi, V., Q. Q. Ruan, and E. Gratton. 2005. 3-D particle tracking in a two-photon microscope: application to the study of molecular dynamics in cells. *Biophys. J.* 88:2919–2928.
15. Ghislain, L. P., and W. W. Webb. 1993. Scanning-force microscope based on an optical trap. *Opt. Lett.* 18:1678–1680.
16. Lang, M. J., C. L. Asbury, J. W. Shaevitz, and S. M. Block. 2002. An automated two-dimensional optical force clamp for single molecule studies. *Biophys. J.* 83:491–501.
17. Rohrbach, A., and E. H. K. Stelzer. 2002. Three-dimensional position detection of optically trapped dielectric particles. *J. Appl. Phys.* 91: 5474–5488.
18. Rohrbach, A., and E. H. K. Stelzer. 2002. Trapping forces, force constants, and potential depths for dielectric spheres in the presence of spherical aberrations. *Appl. Opt.* 41:2494–2507.
19. Rohrbach, A., H. Kress, and E. H. K. Stelzer. 2003. Three-dimensional tracking of small spheres in focused laser beams: influence of the detection angular aperture. *Opt. Lett.* 28:411–413.
20. Amblard, F., B. Yurke, A. Pargellis, and S. Leibler. 1996. A magnetic manipulator for studying local rheology and micromechanical properties of biological systems. *Rev. Sci. Instrum.* 67:818–827.
21. Assi, F., R. Jenks, J. Yang, C. Love, and M. Prentiss. 2002. Massively parallel adhesion and reactivity measurements using simple and inexpensive magnetic tweezers. *J. Appl. Phys.* 92:5584–5586.
22. Barbic, M., J. J. Mock, A. P. Gray, and S. Schultz. 2001. Scanning probe electromagnetic tweezers. *Appl. Phys. Lett.* 79:1897–1899.
23. Fisher, J. K., J. Cribb, K. V. Desai, L. Vicci, B. Wilde, K. Keller, R. M. Taylor, J. Haase, K. Bloom, E. T. O'Brien, and R. Superfine. 2006. Thin-foil magnetic force system for high-numerical-aperture microscopy. *Rev. Sci. Instrum.* 77:023702.
24. Gosse, C., and V. Croquette. 2002. Magnetic tweezers: micromanipulation and force measurement at the molecular level. *Biophys. J.* 82: 3314–3329.
25. Haber, C., and D. Wirtz. 2000. Magnetic tweezers for DNA micromanipulation. *Rev. Sci. Instrum.* 71:4561–4570.
26. Huang, H., C. Y. Dong, H. S. Kwon, J. D. Sutin, R. D. Kamm, and P. T. So. 2002. Three-dimensional cellular deformation analysis with a two-photon magnetic manipulator workstation. *Biophys. J.* 82:2211–2223.
27. Strick, T. R., J. F. Allemand, D. Bensimon, A. Bensimon, and V. Croquette. 1996. The elasticity of a single supercoiled DNA molecule. *Science.* 271:1835–1837.
28. Valberg, P. A., and D. F. Albertini. 1985. Cytoplasmic motions, rheology, and structure probed by a novel magnetic particle method. *J. Cell Biol.* 101:130–140.
29. Ziemann, F., J. Radler, and E. Sackmann. 1994. Local measurements of viscoelastic moduli of entangled actin networks using an oscillating magnetic bead micro-rheometer. *Biophys. J.* 66:2210–2216.
30. Liu, Y., D. K. Cheng, G. J. Sonek, M. W. Berns, C. F. Chapman, and B. J. Tromberg. 1995. Evidence for localized cell heating induced by infrared optical tweezers. *Biophys. J.* 68:2137–2144.
31. Peterman, E. J. G., F. Gittes, and C. F. Schmidt. 2003. Laser-induced heating in optical traps. *Biophys. J.* 84:1308–1316.
32. Schonle, A., and S. W. Hell. 1998. Heating by absorption in the focus of an objective lens. *Opt. Lett.* 23:325–327.
33. Vermeulen, K. C., J. van Mameren, G. J. M. Stienen, E. J. G. Peterman, G. J. L. Wuite, and C. F. Schmidt. 2006. Calibrating bead displacements in optical tweezers using acousto-optic deflectors. *Rev. Sci. Instrum.* 77:013704–013706.
34. Kleinbaum, D. G., L. L. Kupper, and K. E. Muller. 1988. Applied Regression Analysis and Other Multivariable Methods, 2nd ed. PWS-Kent Pub, Boston, MA. 228–250.
35. Born, M., and E. Wolf. 1980. Principles of Optics: Electromagnetic Theory of Propagation, Interference and Diffraction of Light, 6th. ed. Pergamon Press, Oxford.
36. Pralle, A., M. Prummer, E. L. Florin, E. H. Stelzer, and J. K. Horber. 1999. Three-dimensional high-resolution particle tracking for optical tweezers by forward scattered light. *Microsc. Res. Tech.* 44:378–386.
37. Feitosa, M. I. M., and O. N. Mesquita. 1991. Wall-drag effect on diffusion of colloidal particles near surfaces: a photon correlation study. *Phys. Rev. A.* 44:6677.
38. Saxton, M. J., and K. Jacobson. 1997. Single-particle tracking: applications to membrane dynamics. *Annu. Rev. Biophys. Biomol. Struct.* 26:373–399.
39. Mason, T. G., K. Ganesan, J. H. van Zanten, D. Wirtz, and S. C. Kuo. 1997. Particle tracking microrheology of complex fluids. *Phys. Rev. Lett.* 79:3282–3285.
40. Mathlouthi, M., and J. Génotelle. 1995. Rheological Properties of Sucrose Solutions and Suspensions. Blackie Academic & Professional, London.
41. Caspi, A., R. Granek, and M. Elbaum. 2002. Diffusion and directed motion in cellular transport. *Phys. Rev. E.* 66:011916.

42. Ragsdale, G. K., J. Phelps, and K. Luby-Phelps. 1997. Viscoelastic response of fibroblasts to tension transmitted through adherens junctions. *Biophys. J.* 73:2798–2808.

43. Tseng, Y., T. P. Kole, and D. Wirtz. 2002. Micromechanical mapping of live cells by multiple-particle-tracking microrheology. *Biophys. J.* 83:3162–3176.

44. Nan, X., P. A. Sims, P. Chen, and X. S. Xie. 2005. Observation of individual microtubule motor steps in living cells with endocytosed quantum dots. *J. Phys. Chem. B.* 109:24220–24224.

45. Daniels, B. R., B. C. Masi, and D. Wirtz. 2006. Probing single-cell micromechanics in vivo: the microrheology of C. elegans developing embryos. *Biophys. J.* 90:4712–4719.

46. Yamada, S., D. Wirtz, and S. C. Kuo. 2000. Mechanics of living cells measured by laser tracking microrheology. *Biophys. J.* 78:1736–1747.

47. Tolic-Norrelykke, I. M., E.-L. Munteanu, G. Thon, L. Oddershede, and K. Berg-Sorensen. 2004. Anomalous diffusion in living yeast cells. *Phys. Rev. Lett.* 93:078102–078104.

48. Golding, I., and E. C. Cox. 2006. Physical nature of bacterial cytoplasm. *Phys. Rev. Lett.* 96:098102–098104.

49. Wolfgang, F., W. Monika, and S. Erich. 2001. Dictyostelium cells' cytoplasm as an active viscoplastic body. *Eur. Biophys. J.* V30: 284–294.

50. Wilhelm, C., F. Gazeau, and J. C. Bacri. 2003. Rotational magnetic endosome microrheology: viscoelastic architecture inside living cells. *Phys. Rev. E.* 67:061908–061912.

51. Gittes, F., and F. C. MacKintosh. 1998. Dynamic shear modulus of a semiflexible polymer network. *Phys. Rev. E.* 58:R1241.

52. Morse, D. C. 1998. Viscoelasticity of tightly entangled solutions of semiflexible polymers. *Phys. Rev. E.* 58:R1237.

53. Erwin, F. 2002. Physics in cell biology: on the physics of biopolymers and molecular motors. *ChemPhysChem.* 3:270–275.

54. Doi, M., and S. F. Edwards. 1986. The Theory of Polymer Dynamics. Oxford University Press, New York.

55. Schnurr, B., F. Gittes, F. C. MacKintosh, and C. F. Schmidt. 1997. Determining microscopic viscoelasticity in flexible and semiflexible polymer networks from thermal fluctuations. *Macromolecules.* 30: 7781–7792.

56. Janmey, P. A., U. Euteneuer, P. Traub, and M. Schliwa. 1991. Viscoelastic properties of vimentin compared with other filamentous biopolymer networks. *J. Cell Biol.* 113:155–160.

57. Leterrier, J. F., J. Kas, J. Hartwig, R. Vegners, and P. A. Janmey. 1996. Mechanical effects of neurofilament cross-bridges. Modulation by phosphorylation, lipids, and interactions with f-actin. *J. Biol. Chem.* 271:15687–15694.

58. Ma, L., J. Xu, P. A. Coulombe, and D. Wirtz. 1999. Keratin filament suspensions show unique micromechanical properties. *J. Biol. Chem.* 274:19145–19151.

59. Coulombe, P. A., O. Bousquet, L. Ma, S. Yamada, and D. Wirtz. 2000. The 'ins' and 'outs' of intermediate filament organization. *Trends Cell Biol.* 10:420–428.

60. Mucke, N., L. Kreplak, R. Kirmse, T. Wedig, H. Herrmann, U. Aebi, and J. Langowski. 2004. Assessing the flexibility of intermediate filaments by atomic force microscopy. *J. Mol. Biol.* 335:1241–1250.

61. Kusumi, A., Y. Sako, and M. Yamamoto. 1993. Confined lateral diffusion of membrane receptors as studied by single particle tracking (nanovid microscopy). Effects of calcium-induced differentiation in cultured epithelial cells. *Biophys. J.* 65:2021–2040.

62. Kusumi, A., and Y. Sako. 1996. Cell surface organization by the membrane skeleton. *Curr. Opin. Cell Biol.* 8:566–574.

63. Edidin, M., S. C. Kuo, and M. P. Sheetz. 1991. Lateral movements of membrane glycoproteins restricted by dynamic cytoplasmic barriers. *Science.* 254:1379–1382.

64. Chen, Y., W. R. Thelin, B. Yang, S. L. Milgram, and K. Jacobson. 2006. Transient Anchorage of Cross-Linked Glycosyl-Phosphatidylinositol-Anchored Proteins Depends on Cholesterol, Src Family Kinases, Caveolin, and Phosphoinositides. Rockefeller University Press, New York. 169.

65. Weisberg, S. 1985. Applied Linear Regression. Wiley, New York.